Available online at www.sciencedirect.com
SCIENCE DIRECT
Acta Materialia 54 (2006) 3407–3416
Acta MATERIALIA
www.actamat-journals.com

# The glide of screw dislocations in bcc Fe: Atomistic static and dynamic simulations ☆

Julien Chaussidon, Marc Fivel, David Rodney *

*Génie Physique et Mécanique des Matériaux (UMR CNRS 5010), Institut National Polytechnique de Grenoble, 101 rue de la Physique, 38402 Saint Martin d'Hères, France*

Received 12 October 2005; received in revised form 24 February 2006; accepted 23 March 2006
Available online 19 June 2006

**Abstract**

We present atomic-scale simulations of screw dislocation glide in bcc iron. Using two interatomic potentials that, respectively, predict degenerate and non-degenerate core structures, we compute the static 0 K dependence of the screw dislocation Peierls stress on crystal orientation and show strong boundary condition effects related to the generation of non-glide stress components. At finite temperatures we show that, with a non-degenerate core, glide by nucleation/propagation of kink-pairs in a {1 1 0} glide plane is obtained at low temperatures. A transition in the twinning region, towards an average {1 1 2} glide plane, with the formation of debris loops is observed at higher temperatures.


*Keywords:* Molecular dynamics; Dislocation mobility; Iron

## 1. Introduction

The origin for the specific plastic behavior of bcc metals at low temperatures can be traced down to the non-planar extended core configuration of the screw dislocations in these materials [1]. The latter configuration implies a large value for the lattice-friction Peierls stress, overcome by the gliding screw dislocations with the help of thermal activation. In the present paper, bcc α-Fe is of specific interest.

At the macroscopic scale, plastic properties of bcc metals have been extensively studied, mostly by means of uniaxial tension/compression tests (for a review, see Ref. [2]; for α-Fe, see Refs. [3–5]). A key observation is that, at low temperature, bcc metals do not follow the Schmid law, which states that glide on a given slip system starts when the Resolved Shear Stress (RSS) on that system reaches a critical value. There are two types of deviations [6]: first, the critical RSS depends on the sign of the applied stress (which is a consequence of the twinning/antitwinning asymmetry of the bcc lattice), and second, the critical RSS is influenced by non-glide components of the applied stress tensor. The latter are of two types [7]: shear stresses in the Burgers vector direction acting on planes other than the glide plane, and shear stresses perpendicular to the Burgers vector.

At the atomic scale, the study of bcc screw dislocations was one of the first applications of atomistic simulations to plasticity (see [8]; for a recent review, see [9]). However, one has to be cautious about the results of these simulations for several reasons. First, different interatomic potentials may predict different core structures, even for the same material [6,10,11]. In the case of α-Fe, earlier simulations using pair potentials [8] and later calculations with many-body embedded atom method (EAM) potentials [12,13] predicted a *degenerate* core, spread asymmetrically on the three {1 1 0} planes of the [1 1 1] zone, yielding two distinct

☆ This manuscript was presented at the "Micromechanics and Microstructure Evolution: Modeling, Simulation and Experiments" held in Madrid/Spain, September 11–16, 2005.

* Corresponding author. Tel.: +33 4 76 82 63 37; fax: +33 4 76 82 63 82.
*E-mail address:* david.rodney@inpg.fr (D. Rodney).

1359-6454/$30.00 
doi:10.1016/j.actamat.2006.03.044

and equivalent configurations related by a diadic symmetry around a ⟨1 1 0⟩ axis normal to the dislocation line. However, more recent and accurate structure calculations based on the density functional theory (DFT) yielded a *non-degenerate* core [14], spread symmetrically into the three {1 1 0} planes. This structure is now predicted by the latest EAM potentials [15].

Second, most atomic-scale simulations in α-Fe [12,13] cannot be reconciled with experiments because they predict average {1 1 2} glide planes, while experimentally at low temperature, glide is observed on {1 1 0} planes (except when the Maximum Resolved Shear Stress Plane (MRSSP) is close to {1 1 2}) [3]. In particular with degenerate cores, even if in most simulations the MRSSP is a {1 1 0} plane, the screw dislocations glide on an average {1 1 2} plane by elementary steps on two {1 1 0} planes.

Finally, dynamic simulations at finite temperature are computationally expensive because accurate results require large 3D simulation cells, with long dislocation segments in order to capture double-kink nucleation/propagation events, which are the finite temperature glide mechanism. Most simulations are therefore static and quasi-2D. Only recently [13] were large 3D simulations performed, with a potential yielding a degenerate core. This study confirmed the double-kink mechanism with an average {1 1 2} twinning glide plane.

In the present article, we employ two EAM potentials [15,16] that predict the two types of dislocation cores, and characterize both the static and dynamic properties of the screw dislocations modeled by these potentials. In the static case (Section 3), we compute the Peierls stress as a function of crystal orientation and show strong boundary condition effects. In the dynamical case (Section 4), we perform a series of large 3D MD simulations for a range of temperatures and applied stresses and show in particular that, with a non-degenerate core, the glide plane is the {1 1 0} MRSSP at low temperatures, with a transition towards the {1 1 2} twinning plane at higher temperatures and stresses. The relevance of the present simulations to experimental data and previous works published in the literature is finally discussed (Section 5).

## 2. Computational model

### 2.1. Crystallography

The simulation cell used here is schematically shown in Fig. 1(a). Its orientation around the $Y = [1\,1\,1]$ axis which is the close-packed Burgers vector direction, is defined by the angle $\chi$ between the horizontal MRSSP of the cell and the $(\bar{1}\,0\,1)$ plane, used as a reference (as will be detailed below, the boundary conditions produce a $\sigma_{YZ}$ shear stress with horizontal MRSSP). The MD simulations were performed in a cell with $\chi = 0$, i.e. horizontal $(\bar{1}\,0\,1)$ planes. In the static simulations, we computed the dependence of the Peierls stress on the crystal orientation by rotating the cell around the $Y$-axis. Fig. 1(b) presents the plane

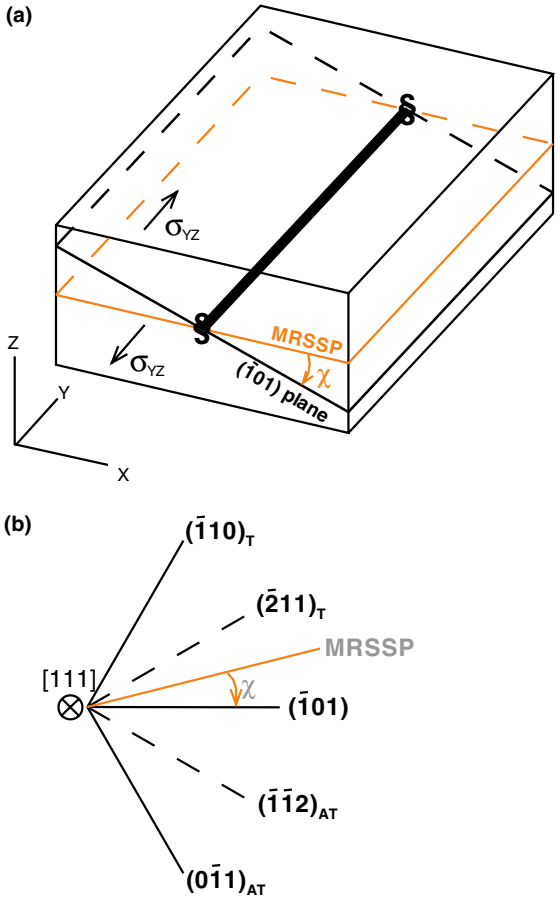


Fig. 1. Definition of the angle $\chi$ (a) in the simulation cell and (b) with respect to the {1 1 0} and {1 1 2} planes of the [1 1 1] zone.

indexes of the [1 1 1] zone and recalls that three {1 1 0} and three {1 1 2} planes intersect along the [1 1 1] direction and that each {1 1 0} plane is bordered by two {1 1 2} planes and vice versa. Because of the symmetries of the bcc lattice, all orientations are considered if $\chi$ is varied between ±30°, but because of the asymmetry of shear parallel to {1 1 2} planes, positive and negative $\chi$ angles are not equivalent. In the simulations, only positive $\sigma_{YZ}$ shear stresses are applied, such that the $(\bar{2}\,1\,1)$ planes are sheared in the twinning sense, while the $(\bar{1}\,\bar{1}\,2)$ planes in the antitwinning sense (see Ref. [10] for more details). We will refer to the region $\chi < 0$ (resp. $\chi > 0$) as the twinning (resp. antitwinning) region and will use subscripts T and AT to recall to which region the planes belong. Each {1 1 0} plane is thus bordered by two {1 1 2} planes, one sheared in the twinning sense, the other, in the antitwinning sense.

### 2.2. Boundary conditions

The cell dimensions used here are $L_X = 25.2$ nm, $L_Z = 13.1$ nm in the $X$ and $Z$ directions, respectively. Along the dislocation line, the static simulations were quasi-2D with $L_Y = 2.5$ nm while for the dynamic simulations, in order to capture the double-kink mechanism, we

needed long dislocation segments and employed $L_Y = 64.2$ nm.

We tested different types of boundary conditions. In all cases, periodic boundary conditions were applied in the $Y$-direction along the dislocation line and free boundary conditions in the $X$-direction. In the $Z$-direction, we applied either full or modified free boundary conditions. In the latter case, referred to as *2D-dynamics*, atoms lying in slabs of width equal to the potential cut-off distance from the upper and lower $Z$ surfaces are fixed in the $Z$-direction and free to move in the $X$ and $Y$ directions. This type of boundary conditions has been used in fcc metals (see Ref. [17,18] and references therein). It can be viewed as *Rigid* in the $Z$-direction but allows to apply stress-controlled boundary conditions. An $a/2[1\,1\,1]$ screw dislocation is introduced in the center of the cell, along the $Y$-direction, by means of its elastic displacement field.

In order to force the screw dislocation to glide, we apply stress-controlled boundary conditions by superimposing to the atoms in the upper and lower slabs (as defined above) constant and opposite forces in the $Y$-direction, in order to produce a $\sigma_{YZ}$ external shear stress. As said in previous section, only positive shear stresses were applied.

Atomic configurations are visualized either by differential displacement maps [8] where first-neighbor [1 1 1] atomic columns are linked by arrows of length proportional to their relative displacement in the Burgers vector direction, or by a first-neighbor analysis [18] where are shown only those atoms which do not have 8 first neighbors close to perfect bcc positions. The latter atoms are called *core atoms* in the following.

### 2.3. Interatomic potentials

We employ two iron interatomic EAM potentials. One potential was developed by Simonelli et al. [16] in order to describe α-Fe crystals and has been used for example to study twin nucleation at crack tips [19]. The other more recent potential was developed by Mendelev et al. [15] (Potential 2 in the reference) in order to describe crystalline as well as liquid iron by including in the fitting procedure first-principle forces obtained on a model liquid configuration. In the following, the potential developed by Simonelli et al. (resp. Mendelev et al.) will be noted *potential S* (resp. *M*).

We computed the kink-pair formation energy predicted by both potentials and found very contrasted results. Potential *M* predicts high values of 0.67 eV for the vacancy-type kink and 1.02 eV for the interstitial-type kink, while potential *S* predicts a low and identical value for both kinks, equal to 0.2 eV. The value extrapolated from experimental data is 0.8 eV for the kink pair [12], i.e. about twice that of potential *S* and half that of potential *M*.

Fig. 2 presents the differential displacement maps of the screw dislocation cores obtained with both potentials. As can be seen, potential *S* predicts a degenerate core, asymmetrically spread in the three {1 1 0} of the [1 1 1] zone. Potential *M* predicts a non-degenerate symmetric core (close to the elastic solution) in close agreement with recent DFT calculations [14]. We will use this fundamental difference to study the influence of the core structure both on the static and dynamic properties of a screw dislocation. Note also for later use that the stable configuration (called *soft*) of the dislocation cores shown here is centered on a triangle pointing downward in this [1 1 1] projection. There exists also an unstable configuration (called *hard*) where the core is centered on an upward triangle (see Ref. [8] for details).

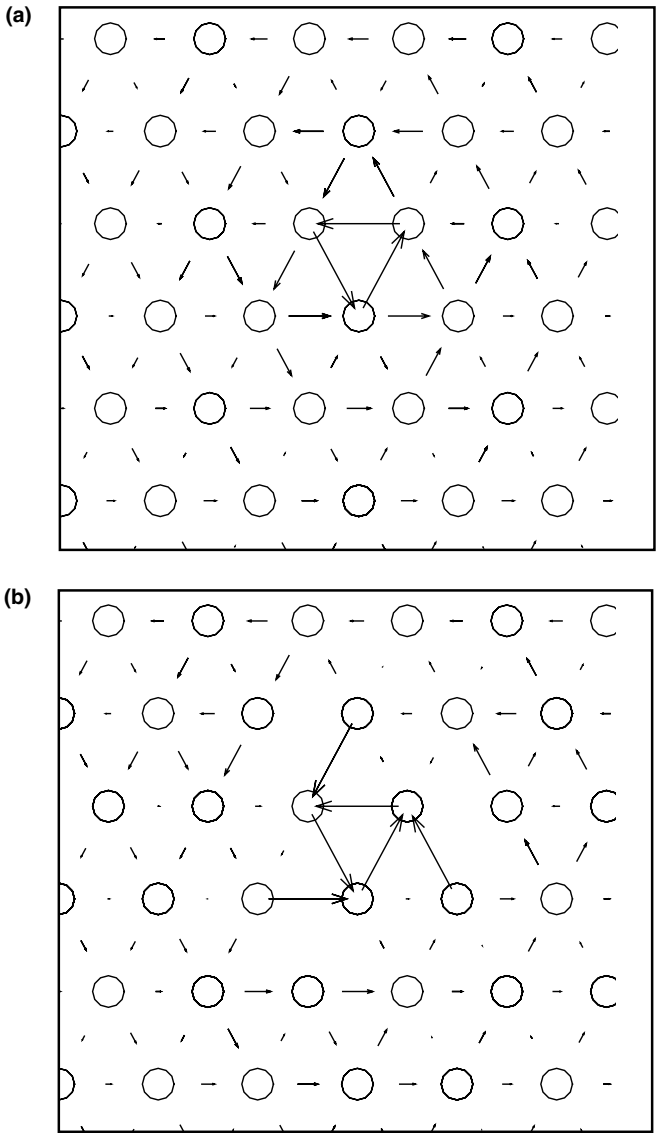


Fig. 2. Differential displacement maps of screw dislocation cores showing (a) the non-degenerate structure of Mendelev et al. potential [15] and (b) the degenerate structure of Simonelli et al. potential [16].

## 3. Static properties and boundary effects

We consider here the dependence of the Peierls stress of the $a/2[1\,1\,1]$ screw dislocation on crystal orientation. We performed static simulations by increasing the applied

stress incrementally and relaxing the configuration between each increment. The energy-minimization algorithm used here is based on zeroing atomic velocities whenever their dot product with the atomic force is negative.

With potential $M$, the Peierls stress is well defined since, when the applied stress is increased, there is a critical stress below which the dislocation is stable, and above which dislocation motion is unbounded. By way of contrast, there are two critical stresses with potential $S$: when the applied stress reaches a lower critical stress, the dislocation advances by one atomic distance, adopts a metastable configuration and remains fixed until a second upper critical stress is reached, above which the motion becomes unbounded. Double critical stresses were found with other potentials (see, for example, Ref. [20]). Whenever Peierls stresses are shown with potential $S$, both critical stresses are shown.

Fig. 3(a) shows the evolution of the Peierls stress as a function of the crystal orientation $\chi$ obtained with potential $M$ employing either free boundary conditions or 2D dynamics in the $Z$-direction. The plane on which the dislocation glided is noted in the figure.

We see a strong influence of the boundary conditions both on the numerical values of the Peierls stress and on the glide plane selection. For $\chi < 0$ with 2D dynamics, the dislocation glides on a $(\bar{2}11)_T$ plane (empty symbols in Fig. 3(a)), while with free boundary conditions, the dislocation glides on a $(\bar{1}01)$ plane for all orientations plain symbols in Fig. 3(a)) except when $\chi$ is close to $-30°$, i.e. when the MRSSP is close to $(\bar{2}11)_T$. Numerically, in the region $\chi > 0$ where in both cases the dislocation glides on $(\bar{1}01)$, the Peierls stress with 2D dynamics is about 300 MPa lower than that obtained with free boundary conditions. Note also that the Peierls stress is discontinuous when the glide plane changes from $(\bar{1}01)$ to $(\bar{2}11)_T$. The Peierls stress for $\chi = +30°$, i.e. when the MRSSP is $(\bar{1}\,\bar{1}\,2)_{AT}$, is not reported on the figure because it is unrealistically high (about 5.4 GPa) and in that case, the plastic deformation is not due to a dislocation but rather to a plate of intense shear.

This strong influence of the boundary conditions is due to a shear/tension coupling associated to the twinning/antitwinning asymmetry of shear on {1 1 2} planes. Indeed, the bcc lattice is not symmetrical with respect to {1 1 2} planes: the [1 1 1] atomic columns are shifted by $b/3$ with respect to each other, with reference positions $-b/3$, 0, $b/3$,... When the lattice is sheared parallel to a {1 1 2} plane, the reference positions of the columns become $-b/3 - e$, 0, $b/3 + e$, with $e > 0$ (resp. $e < 0$) when the crystal is sheared in the twinning (resp. antitwinning) sense and thus, the distance between atoms in the neighboring [1 1 1] columns increases (resp. decreases). Correspondingly, in the twinning case, the lattice tends to compress perpendicularly to the {1 1 2} plane, while in the antitwinning case, it expands. The 2D dynamical boundary conditions forbid these expansion and contraction because they are rigid in the $Z$-direction and no out-of-plane motion is allowed in the upper and lower crystal surfaces. Tensile stresses in the $Z$-direction are thus generated which in turn produce shear components perpendicular to the Burgers vector of the screw dislocation. As said in Section 1, these non-glide components are known to affect the Peierls stress [7] and are at the origin of the differences observed between the two boundary conditions. In Fig. 3(a), the 2 curves cross at $\chi = 0$, i.e. when the MRSSP is $(\bar{1}01)$ because it is the only orientation for which shear is symmetrical and no stress is generated in the $Z$-direction with 2D dynamics. Note also that the shear/tension coupling is volumic and its effect is therefore independent of the size of the simulation cell. In fact, this coupling is found in any crystal with cubic symmetries: a shear deformation $\epsilon_{YZ}$ with $Y = [1\,1\,1]$ and $Z = [\bar{1}\,\bar{1}\,2]$ applied to a crystal with cubic symmetries (and elastic constants $c_{11}$, $c_{12}$, $c_{44}$) produces a stress tensor

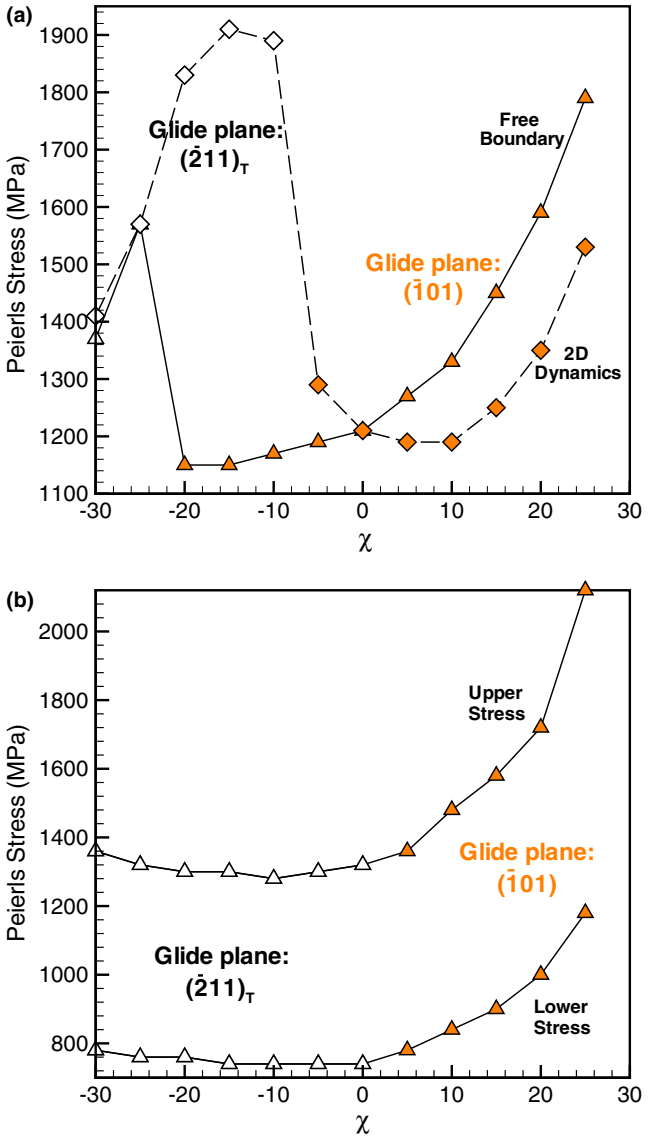


Fig. 3. Variation of Peierls stress with crystal orientation for 2 EAM potentials: (a) potential $M$ where two boundary conditions are compared (free boundary or 2D-dynamics), and (b) potential $S$ where the upper and lower critical stresses are shown.

with a component $\sigma_{ZZ} = \sqrt{2}/3(-c_{11} + c_{12} + 2c_{44})\epsilon_{YZ}$, thus showing the coupling between the shear $\epsilon_{YZ}$ and the tension $\sigma_{ZZ}$ in the direction perpendicular to the plane of application of the shear.

Fig. 3(b) shows the evolution of the Peierls stress obtained with potential $S$ and free boundary conditions. Both the lower and upper Peierls stresses are noted on the figure, the lower stress being about 600 MPa below the upper one. The latter is close to the Peierls stress obtained with potential $M$. The glide plane is $(\bar{1}01)$ in the antitwinning region and $(\bar{2}11)_T$ in the twinning region. Note that with the present potential, the Peierls stress is continuous at the transition between glide planes. Also, the Peierls stress is almost constant in the twinning region.

Fig. 4 illustrates the well-known fact that the Peierls stress in bcc crystals does not obey the $\chi$-dependence of Schmid law. Fig. 4 reproduces the data obtained with potential M in the region where the dislocation glides on $(\bar{1}01)$. First, the twinning/antwinning asymmetry is clearly visible when comparing the regions $\chi > 0$ and $\chi < 0$. Second, the dashed curve is Schmid law $(\sigma_P^o/\cos(\chi))$ fitted on the Peierls stress at $\chi = 0$. We see in particular that the Peierls stress in the region $\chi > 0$ decreases much faster than Schmid law and does not increase for $\chi < 0$. The solid curve is the fit obtained using the effective yield stress criterion proposed by Vitek et al. [21], who suggested that the effect of non-glide resolved shear stresses on planes other than the glide plane should be accounted for in the form of a linear combination. Based on their simulations, they found that the important shear stress is that acting on $(\bar{1}10)_T$. With our notations, the Peierls stress is then expressed as:

$$\sigma_P = \frac{\sigma_P^o}{\cos(\chi) + a \cdot \cos(60 + \chi)} \quad (1)$$

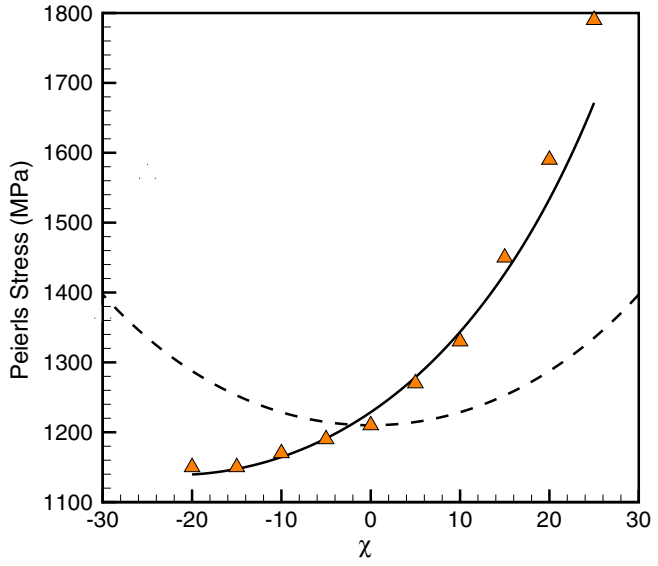


Fig. 4. Comparison between Schmid law (dashed curve) and an effective Peierls stress relation (solid curve) [21].

Fig. 4 shows that this fit with $\sigma_P^o = 1604$ MPa and $a = 0.61$ improves greatly the prediction of the Peierls stress, except in the region close to 30°, which could be due to the unrealistic Peierls stress for $\chi = 30°$.

## 4. Dynamic properties

We performed a series of large 3D MD simulations with a 64 nm-long screw dislocation in a cell with $(\bar{1}01)$ MRSSP. In this section, we will focus mainly on simulations performed with potential $M$. The duration of the simulations was set to 100 ps. The temperature was varied in the range 50–150 K, i.e. within the experimental range where plasticity is dominated by the thermally activated motion of screw dislocations. No temperature control was used, because the dislocation glides over limited distances and the temperature raises by less than 2 K. The applied stress was varied in the range 200–700 MPa, i.e. well below the Peierls stress, which is 1210 MPa for this $\chi = 0$ orientation (see Fig. 3(a)). Free boundary conditions are applied in $X$ and $Z$ directions (see Fig. 1(a)). From the energy of the dislocation as a function of its position in the cell, we found that the image stress on the dislocation produced by the free surfaces is below 50 MPa for glide distances below 25 Peierls valleys. The results presented hereafter are thus computed within this range. The dislocation is first relaxed at 0 K under the desired stress before the target temperature is set and the MD simulation started.

Fig. 5 is a map of the dislocation average velocity and average glide-plane angle $\psi$ with respect to the horizontal $(\bar{1}01)$ MRSSP. A similar velocity map was obtained by

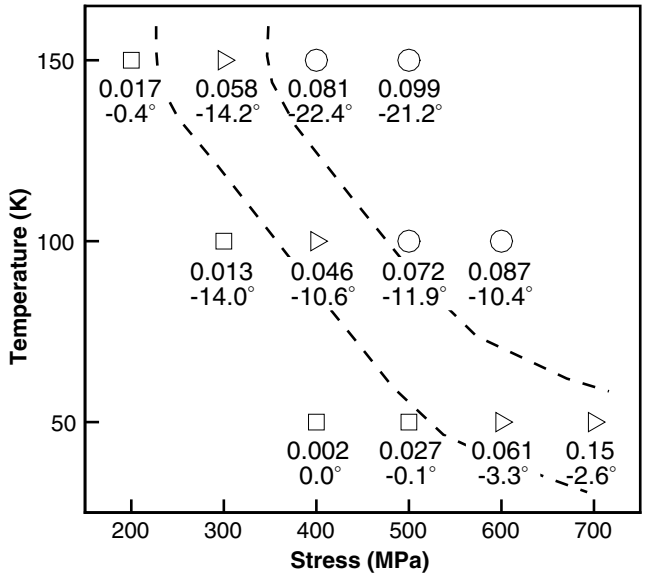


Fig. 5. Map of the dislocation average velocity and glide-plane angle $\psi$ with respect to the horizontal $(\bar{1}01)$ MRSSP. For each temperature and applied stress condition, the velocity is given in nm ps$^{-1}$ and the corresponding angle in degrees. Squares, right-triangles and circles refer to glide regimes: single kink pair, multiple kink pair with avalanches and rough multiple kink pair, respectively (see the text for details).

Marian et al. [13] with an EAM potential that predicts a degenerate core structure.

The glide mechanism is the nucleation and propagation of kink pairs in {1 1 0} planes, as illustrated in Fig. 6 which displays dislocation core positions at different times for different stress and temperature conditions. The core was determined by taking the center of gravity of the core atoms (as defined by the first-neighbor analysis presented in Section 2) in slices of width *2b* along the dislocation line.

At low temperatures and stresses, there is a *Single Kink-Pair (SKP) regime* where glide is intermittent with waiting times separated by the nucleation of kink pairs that appear one-by-one and annihilate with themselves through the periodic boundary conditions along the dislocation line. The process, illustrated in Fig. 6(a), occurs by the successive nucleation and propagation of two kink pairs of height $0.5d$, where $d = 2\sqrt{2}b/3$ is the distance between Peierls valleys. The first kink pair brings the dislocation from a stable *soft* position to an unstable *hard* position, while the second kink pair brings the dislocation back into a stable *soft* position, in the next Peierls valley. The *hard* dislocation segment is metastable presumably because of the line tension effect of the edge kinks. The kinks expand with high saturated velocities, of the order of 4.5 nm ps$^{-1}$, mostly independent of the temperature and stress in the range considered here. Also, vacancy-type and interstitial kinks have similar velocities although their formation energies are very contrasted with potential *M*. In the map of Fig. 5, the points corresponding to this SKP regime are noted as squares. This figure shows that the glide plane angle $\psi$ is 0° at 50 K and reaches −14° at 100 K. The reason is the activation of cross-slip with temperature

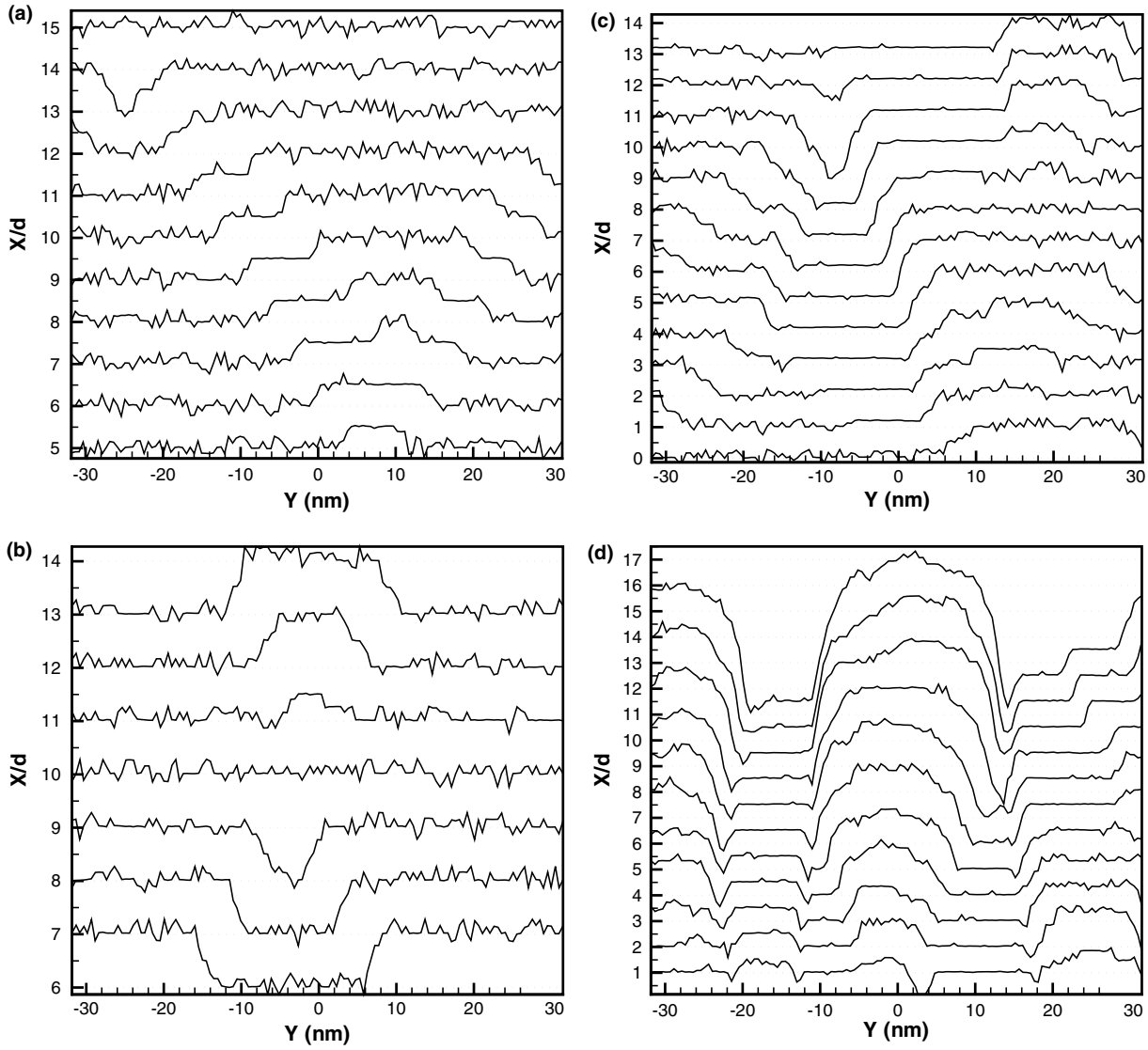


Fig. 6. Dislocation core motion in (a) the single-kink pair regime (300 MPa, 100 K), (b) the single-kink pair regime (500 MPa, 50 K) where a nucleation following an annihilation is shown, (c) the multiple-kink pair regime with avalanches (400 MPa, 100 K) and (d) the rough multiple-kink pair regime (600 MPa, 100 K). The lines connect the centers of gravity of the core atoms along the dislocation line in a $[\bar{1}\,0\,1]$ projection. They are shown every 0.8 ps and, for the sake of clarity, the curves are shifted by *d* with respect to each other, where *d* is the width of the Peierls valley.

(see Section 5) that leads to an increasing proportion of double kinks nucleated in inclined $(\bar{1}10)_T$ planes at $\chi = -60°$ in the twinning region (see Fig. 1(b)). The glide plane is therefore the $(\bar{1}01)$ MRSSP only at low temperatures and rotates towards the twinning region at higher temperatures. In the simulations, as illustrated in Fig. 6(b), we often observe that a new kink pair nucleates within less than a ps at the position where two kinks annihilated, which is due to the energy locally released by the annihilation.

If temperature and/or stress are increased, the kink-pair nucleation rate increases and we observe a transition to a *multiple kink-pair (MKP) regime* where several kink-pairs coexist on the dislocation line. First, there is an *intermediate regime* where dislocation motion is characterized by waiting times separated by avalanches, i.e. rapid successions of kink-pairs, mostly in horizontal $(\bar{1}01)$ planes. An example of such an avalanche is shown in Fig. 6(c). A kink pair first nucleates and, while it expands along the dislocation line, several other kink pairs appear on this initial kink-pair and also propagate along the dislocation line. Usually, the avalanches comprise 2–3 kink pairs. In this intermediate regime, noted as right triangles in Fig. 5, the glide angle is again mostly a function of the temperature and does not exceed $-15°$.

At even higher temperatures and/or stresses, the kink-pair nucleation rate as well as the number of kink pairs in inclined $(\bar{1}10)_T$ planes increase. At 150 K, the latter becomes almost equal to the number of kink pairs in horizontal $(\bar{1}01)$ planes and consequently, the angle $\psi$ approaches $-30°$ (see Fig. 5) and the average glide plane rotates to $(\bar{2}11)_T$. Fig. 6(d) shows the almost simultaneous nucleation of two kink pairs in different $\{110\}$ planes, leading to a self-pinning of the dislocation by a mechanism that was described in details by Marian et al. [13]: when kink pairs on different $\{110\}$ planes intersect, they lock each other and become pinning points for the dislocation, called *cross-kinks* [22]. The dislocation may then unlock by two mechanisms. One was reported by Marian et al. [13] and involves a combination of kink pairs in both $\{110\}$ planes which allows the dislocation to reconnect in a single $\{110\}$ plane. This mechanism results in the formation of two closed loops, one of vacancy-type, the other interstitial. In the present simulations, we observed another mechanism: when the dislocation velocity is slow enough, we see that the cross-kinks are mobile, glide along the dislocation line and annihilate with one another. No debris loops are formed in this case. The driving force of the motion of the cross-kinks can have two origins: (1) the difference in RSS between the kinks in the inclined and the horizontal $\{110\}$ planes and (2) a possible difference in the length of the two kinks [22]. No waiting times are observed in this regime, that was called *rough* by Marian et al. [13] and, as illustrated in Fig. 7(b), a large density of debris loops is left in the wake of the dislocation. As shown in Fig. 6(d), atomic-scale kinks are no more visible, but are more rounded with heights equal to several interatomic distances.

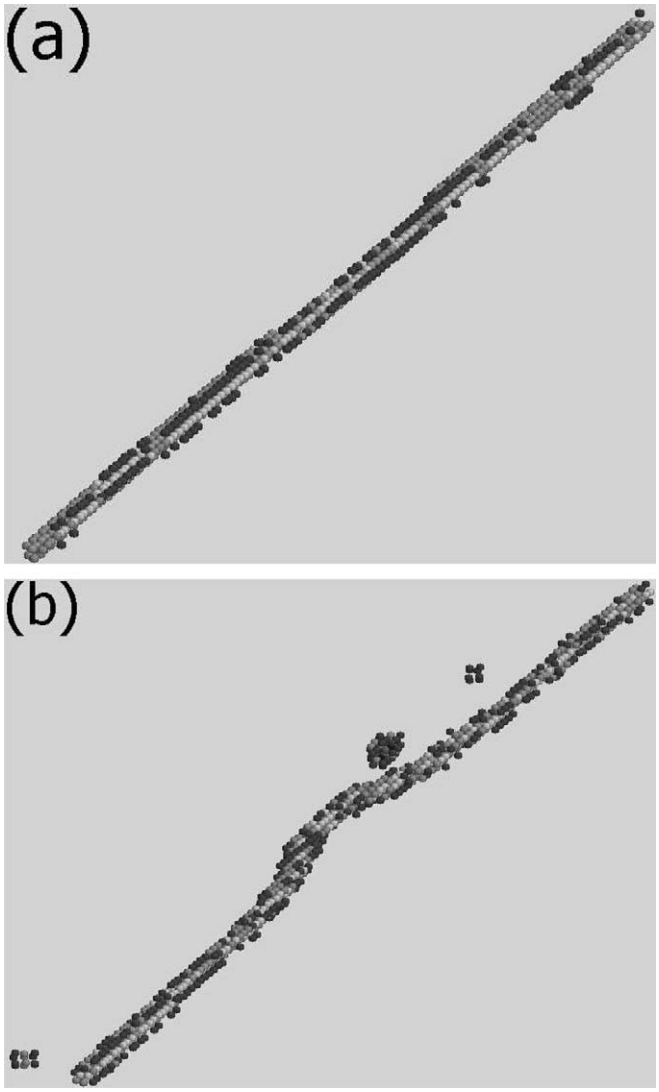


Fig. 7. Core structures obtained with a first-neighbor analysis in (a) the single-kink pair regime (400 MPa, 50 K), (b) the rough multiple-kink pair regime (500 MPa, 150 K).

## 5. Discussion

We identified three regimes: single kink-pair (SKP) regime, multiple kink-pair (MKP) regime with avalanches, and rough multiple kink pair regime, in a window of temperatures and stresses primarily determined by the duration of the simulations: the simulations can be carried out only with temperatures and stresses for which the dislocation advances by several Peierls valleys within 100 ps, which limits us to stress levels higher than in traction/compression tests on single crystals, leading to relatively high dislocation velocities. Such stresses can however easily be reached near heterogeneities, such as cracks, and in small-scale microstructures. Also, note that since the MKP regimes require several kink-pairs along

the dislocation, the stress to enter these regimes will decrease if a longer dislocation line length is used. Finally, the observations made here remain mostly qualitative since we could not perform the number of runs required for accurate statistics due to the computational load of the simulations.

### 5.1. Glide plane predictions for potentials M and S

It is known experimentally that in α-Fe single crystals, slip takes place on $(\bar{1}01)$ planes over the whole temperature range when these planes are MRSSP [3]. Such slip plane is possible if kink-pairs are systematically nucleated in this plane, or if they nucleate in all three $\{1\,1\,0\}$ planes of the $[1\,1\,\bar{1}]$ zone such that, on average, the dislocation glides on $(\bar{1}01)$. At the atomic scale, the first case is compatible only with a non-degenerate core that retains the same configuration after each atomic move and can systematically emit kink pairs in a $(\bar{1}01)$ plane. The present simulations show that indeed, with potential *M* which predicts a non-degenerate core, glide on $(\bar{1}01)$ is possible.

The second option, pencil glide on an average $(\bar{1}01)$ plane, is impossible at least with potential *M*, because we never observed any kink pair nucleating in a $(0\bar{1}1)_{AT}$ plane in the antitwinning region. The glide plane can deviate only towards the twinning region, with no possibility for the dislocation to glide back towards the central $(\bar{1}01)$ plane. To our knowledge, kink pairs on $(0\bar{1}1)_{AT}$ planes have never been observed in atomic-scale simulations.

With a degenerate core such as that predicted by potential *S*, the asymmetry of the two core variants implies that for a given sign of the applied stress and a $(\bar{1}01)$ MRSSP, one variant will emit kink pairs only in a $(\bar{1}01)$ plane (case of the variant shown in Fig. 2(a) if the stress drives the dislocation to the right) while the other variant will emit kink pairs in a $(\bar{1}10)_T$ plane. With degenerate cores, no $(0\bar{1}1)_{AT}$-kink pair have either ever been observed in atomic-scale simulations. The flip from one variant to the other each time the dislocation moves by one Peierls valley implies the nucleation of kink pairs alternatively on $(\bar{1}01)$ and $(\bar{1}10)_T$, resulting on an average $(\bar{2}11)_T$-glide plane, as described in earlier publications [12,13].

### 5.2. Rotation of the glide plane

The map of Fig. 5 shows that the glide plane angle $\psi$ is mostly a function of the temperature and results from the activation with temperature of kink pairs in $(\bar{1}10)_T$ planes. This effect can be understood as least qualitatively from a simple cross-slip model [25] where one assumes that kink pairs nucleate in $(\bar{1}01)$ and $(\bar{1}10)_T$ planes with thermally activated probabilities that depend on the RSS in these planes: $E_0 - V\cdot\sigma$ and $E_0 - V\cdot\sigma/2$, respectively (we thus neglect all non-glide effects). The glide plane angle then follows the relation:

$$\tan(-\psi) = \frac{\sqrt{3}}{1 + 2\exp(V\cdot\sigma/2k_{BT})} \tag{2}$$

With an activation volume $V = 0.45b^3$, we obtain a variation of $\psi$ with temperature of the same order, though less rapid, than observed in the simulations. The cross-slip events may be helped by a change of dislocation core structure. Fig. 8(a) shows the differential displacement map obtained at 500 MPa and 150 K, using atomic positions averaged over 10 ps. We can see in this figure a dissymmetry between the two arrows just above the core triangle, corresponding to an extension of the dislocation core in the inclined $(\bar{1}10)_T$, which favors the nucleation of kink pairs in this plane. The effect is favored by higher stresses since as seen in Fig. 8(b), at 200 MPa and 150 K, the core dissymmetry is much less pronounced.

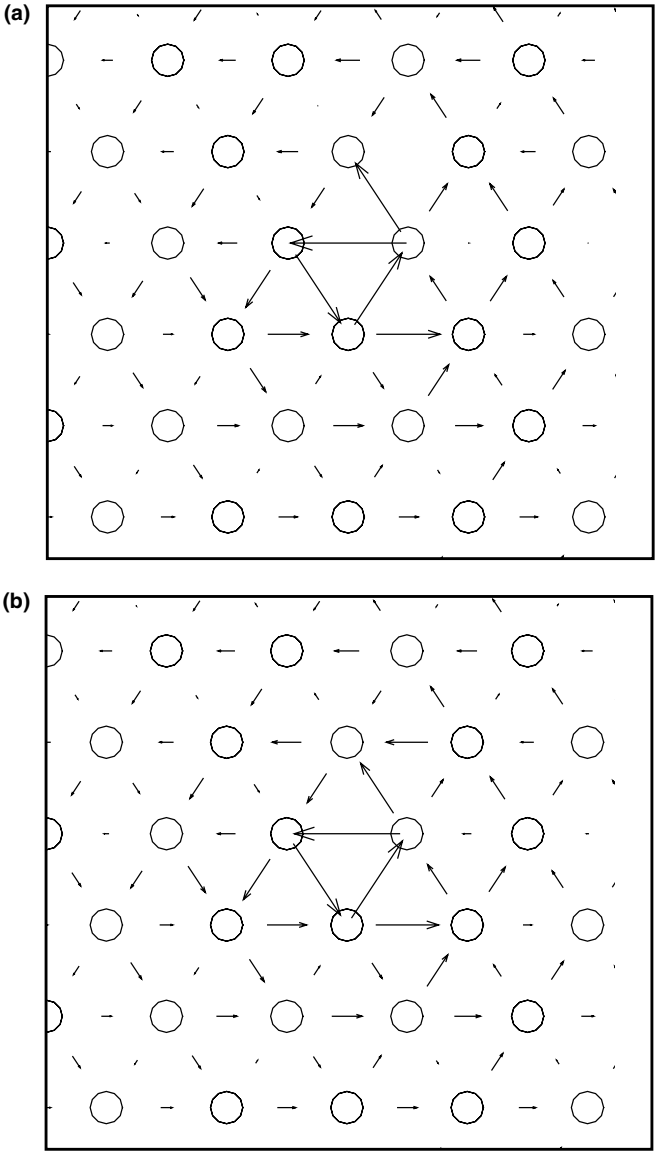


Fig. 8. Average differential displacements of screw dislocation cores at 150 K and (a) 500 MPa, (b) 200 MPa.

The activation with temperature of kink pairs in $(\bar{1}10)_T$ planes is in agreement with the experimental observation that in α-Fe, slip takes place on {1 1 0} at low temperatures (77 K) over the whole orientation range but at higher temperatures, only if the crystal is stressed in the antitwinning region; if the stress is in the twinning region, slip becomes non-crystallographic with an average glide plane parallel to the MRSSP [2,10]. Indeed, combinations of $(\bar{1}01)$- and $(\bar{1}10)_T$-kink pairs can yield any average glide plane in the twinning region, while, in the absence of $(0\bar{1}1)_{AT}$-kink pairs, slip in the antitwinning region can only take place in $(\bar{1}01)$ planes. Similarly, at low temperatures, in absence of $(\bar{1}10)_T$-kink pairs, slip can also take place only in $(\bar{1}01)$ planes. This point should be verified by 3D MD simulations at different temperatures with different crystal orientations.

The present simulations also predict that the slip plane in a crystal oriented with $(\bar{1}01)$ MRSSP should rotate from $(\bar{1}01)$ towards $(\bar{2}11)_T$ when the temperature is increased, which has not been observed experimentally to our knowledge. However, the experimental determination of slip planes [3] was performed on single crystals with low yield stresses below 300 MPa where the evolution of the core structure is not pronounced. An analysis of slip traces in high stress environments, as obtained in small-scale microstructures (for example bainitic steels [24]) would be very informative.

### 5.3. Rough MKP regime

The rough MKP regime requires two conditions: several kinks have to expand simultaneously and in different {1 1 0} planes. The first condition is controlled by the nucleation probability, while the second depends on the core structure.

In the case of a degenerate core, the fact that the variants emit kink pairs in distinct planes makes the coexistence of such kinks difficult and restricts the rough MKP regime (if any) to very high temperatures and stresses. Indeed, using potential *S*, we observed no rough regime over the entire stress and temperature ranges considered here. With this potential, at high stresses, the dislocation core is nearly planar, extended in a $(\bar{2}11)_T$ plane, and the motion appears continuous, with no visible atomic-scale kinks. Marian et al. [13] observed a rough regime with a degenerate core, that can have two reasons: either a change in dislocation core allowing the simultaneous formation of kinks in two {1 1 0} planes or the activation of flips between core variants along the dislocation, as considered by Duesberry [23]. Interestingly, the applied stress for the transition to the rough regime obtained by these authors at low temperature (50 K) is the same as in the present simulations. But, in their case, this transition stress is mostly independent of the temperature while in our case, it is strongly dependent. Also, in agreement with the observations of Marian et al., the interstitial debris loops tend to have large sizes while the vacancies are released one-by-one or in small clusters. Such debris loops were observed in TEM in high yield stress bainitic steels [24], where the RSS is about 450 MPa at 77 K, indicating that in these alloys, the deformation may be in the rough MKP regime, as opposed to single crystals where the applied stress is lower and the deformation is in the SKP regime.

### 5.4. Influence of the boundary conditions

Boundary conditions have a strong influence on the Peierls stress at 0 K as shown in Section 3, when the crystal is sheared in an orientation different from $\chi = 0$, because of the shear–tension coupling associated with the twinning/antitwinning asymmetry. This effect is due to the rigid boundary conditions imposed in the *Z*-direction when 2D dynamics are used. The boundary conditions also affect the selection of the glide plane at finite temperatures. We used 2D-dynamics in the *Z*-direction in MD simulations and found $(\bar{2}11)_T$ glide planes over most of the temperature and stress ranges. In addition, we tested periodic boundary conditions in the *X*-direction and found that these boundary conditions also favor slip in $(\bar{2}11)_T$ planes. Great care must therefore be taken in the choice of the boundary conditions and, from the present simulations, free boundary conditions in both *X* and *Z* directions seem to be the most adapted and rigid boundary conditions should not be used outside the orientation $\chi = 0$.

## 6. Conclusion

The present simulations show that if a potential predicting a non-degenerate core is used, glide at finite temperature on a {1 1 0} plane can be stabilized, in agreement with experimental data and in contrast with MD simulations performed with degenerate cores that predict $\{112\}_T$ average glide planes. For this reason, we believe that, although neither potential *M* nor *S* are physically based models for bcc iron because they do not account for magnetism, potential *M* is more realistic because it stabilizes {1 1 0} glide planes. Also, a transition to a rough regime is obtained with a stronger temperature dependence than with degenerate cores. Finally, the simulation results appear to be very dependent on the boundary conditions, mainly because the latter may produce non-glide stress components that affect dislocation glide.

## Acknowledgments

The authors thank Pr. François Louchet and Dr. Christian Robertson for fruitful discussions, as well as Thomas Nogaret who greatly participated in the development of the parallel MD code used here.

## References


[1] Hirsch P. Proceedings of the fifth international conference on crystallography. Cambridge: Cambridge University Press; 1960. p. 139.
[2] Christian J. Metall Trans A 1983;14:1237.
[3] Spitzig WA, Keh AS. Acta Metall 1970;18:611.
[4] Spitzig WA, Keh AS. Acta Metall 1970;18:1021.
[5] Kuramoto E, Aono Y, Kitajima K, Maeda K, Takeuchi S. Philos Mag A 1979;39:717.
[6] Duesberry M, Vitek V. Acta Mater 1998;46:1481.
[7] Ito K, Vitek V. Philos Mag A 2001;81:1387.
[8] Vitek V. Cryst Latt Def 1974;5:1.
[9] Cai W, Bulatov VV, Chang J, Li J, Yip S. In: Nabarro F, Hirth JP, editors. Dislocations in solids, vol. 12. Amsterdam: Elsevier; 2004. p. 1.
[10] Duesberry M. In: Nabarro F, editor. Dislocations in solids, vol. 8. Amsterdam: North-Holland; 1989. p. 67.
[11] Vitek V. Philos Mag 2004;84:415.
[12] Wen M, Ngan A. Acta Mater 2000;48:4255.
[13] Marian J, Cai W, Bulatov VV. Nat Mater 2004;3:158.
[14] Frederiksen SL, Jacobsen KW. Philos Mag 2003;83:365.
[15] Mendelev MI, Han S, Srolovitz DJ, Ackland GJ, Sun DY, Asta M. Philos Mag 2003;83:3977.
[16] Simonelli G, Pasianot R, Savino E. Mater Res Soc Symp Proc 1993;291:567.
[17] Rodary E, Rodney D, Proville L, Bréchet Y, Martin G. Phys Rev B 2004;70:054111.
[18] Rodney D. Acta Mater 2004;52:607.
[19] Farkas D. Philos Mag 2005;85:387.
[20] Duesberry MS, Vitek V, Bowen DK. Proc R Soc A 1973;332:85.
[21] Vitek V, Mrovec M, Bassani JL. Mat Sci Eng A 2004;365:31.
[22] Louchet F, Viguier B. Philos Mag A 2000;80:765.
[23] Duesberry M. Acta Mater 1984;31:1759.
[24] Obrtlik K, Robertson CF, Marini B. J Nucl Mat 2005;342:35.
[25] The authors thank V.V. Bulatov for this suggestion.